

Systematic upper limits on the size of missing pulsar glitches in the first UTMOST open data release

L. Dunn^{1,2*}, A. Melatos^{1,2}, S. Suvorova^{1,2,3}, W. Moran³, R. J. Evans^{2,3},
S. Osłowski⁴, M. E. Lower^{5,6}, M. Bailes^{5,7}, C. Flynn^{5,7}, V. Gupta⁵

¹*School of Physics, University of Melbourne, Parkville, VIC 3010, Australia*

²*Australian Research Council Centre of Excellence for Gravitational Wave Discovery (OzGrav), University of Melbourne, Parkville, VIC 3010, Australia*

³*Department of Electrical and Electronic Engineering, University of Melbourne, Parkville, VIC 3010, Australia*

⁴*Manly Astrophysics, 15/41-42 East Esplanade, Manly 2095, Australia*

⁵*Centre for Astrophysics and Supercomputing, Swinburne University of Technology, PO Box 218, Hawthorn, Victoria 3122, Australia*

⁶*CSIRO Space and Astronomy, Australia Telescope National Facility, Epping NSW 1710, Australia*

⁷*OzGrav: The ARC Centre of Excellence for Gravitational-wave Discovery, Hawthorn VIC 3122, Australia*

Accepted XXX. Received YYY; in original form ZZZ

ABSTRACT

A systematic, semi-automated search for pulsar glitches in the first UTMOST public data release is presented. The search is carried out using a hidden Markov model which incorporates both glitches and timing noise into the model of the assumed phase evolution of the pulsar. Glitches are detected through Bayesian model selection between models with and without glitches present with minimal human intervention. Nine glitches are detected among seven objects, all of which have been previously reported. No new glitches were detected. Injection studies are used to place 90% frequentist upper limits on the size of undetected glitches in each of the 282 objects searched. The mean upper limit obtained is $\Delta f^{90\%}/f = 1.9 \times 10^{-8}$, with a range of $4.1 \times 10^{-11} \leq \Delta f^{90\%}/f \leq 2.7 \times 10^{-7}$, assuming step events with no post-glitch recoveries. It is demonstrated that including glitch recovery has a mild effect, in most cases increasing the upper limit by a factor of $\lesssim 5$ conservatively assuming complete recovery on a timescale of 100 d.

Key words: pulsars:general – stars:neutron – stars:rotation

1 INTRODUCTION

The secular electromagnetic spindown of a rotation-powered pulsar is sometimes interrupted by a sudden increase in the spin frequency, known as a glitch. Glitches are often but not always accompanied by a change in the secular spin-down rate and a quasi-exponential recovery (Lyne & Graham-Smith 2012). The underlying cause of glitches is unknown (Haskell & Melatos 2015). The standard view of the physical mechanism behind glitches invokes pinning and subsequent unpinning of the vortices of the superfluid neutron component to the lattice of nuclei in the inner crust (Anderson & Itoh 1975), but this broad picture is by no means certain. Long-term statistical analyses have uncovered interesting features of glitch behaviour both in individual objects (Espinoza et al. 2014; Howitt et al. 2018; Carlin & Melatos 2019; Ho et al. 2020) and across the pulsar population (Lyne et al. 2000; Melatos et al. 2008; Espinoza et al. 2011; Yu et al.

2013; Fuentes et al. 2017; Melatos et al. 2018). Note that we distinguish between glitches, which involve a jump in the spin frequency, and events involving abrupt changes in frequency derivative associated with magnetospheric changes (Lyne et al. 2010). Although the latter are glitch-like in some respects and interesting in their own right, they are a distinct class of events and we will not search for them explicitly in this work.

Statistical inferences about the glitch phenomenon rely on the completeness of the catalogues of detected glitches. However, the traditional method of glitch detection, which involves identifying a glitch signature “by eye” in a set of timing residuals (Espinoza et al. 2011; Yu et al. 2013), makes it difficult to assess completeness systematically. Espinoza et al. (2014) and Yu & Liu (2017) employed automated glitch detection methods to evaluate detectability limits. The technique presented by Espinoza et al. (2014) has been applied to timing data from the Crab and Vela pulsars (Espinoza et al. 2021), while the technique presented by Yu & Liu (2017) was tested on simulated data but not used to search for glitches

* E-mail: liamd@student.unimelb.edu.au

in real datasets. Most recently, [Singha et al. \(2021\)](#) have developed a real-time glitch detection pipeline which operates with minimal human intervention and incorporated it into the timing programme at the Ooty Radio Telescope. [Singha et al. \(2021\)](#) reported initial tests of detectability limits with this pipeline, and as more data become available a clearer picture will emerge of the completeness of the glitch sample reported as part of this programme.

[Melatos et al. \(2020\)](#) developed a complementary method for pulsar glitch detection which tracks the pulse frequency and frequency derivative with a hidden Markov model (HMM)¹. The HMM selects between models with and without glitches within a Bayesian framework, complementing model selection studies with TEMPO2 ([Lentati et al. 2014; Shannon et al. 2016; Parthasarathy et al. 2019; Lower et al. 2020](#)). The HMM dynamics include secular spin down and stochastic spin wandering (“timing noise”), as well as step changes associated with glitches ([Melatos et al. 2020](#)). As the HMM detects glitches without human intervention, it is well-suited to analysing a large number of pulsar timing datasets. Its speed makes it practical to do injection studies to obtain upper limits on the size of undetected glitches, and hence quantify the completeness of the existing and new catalogues.

In this work we search for glitches in the datasets released as part of the UTMOST pulsar timing programme ([Jankowski et al. 2019; Lower et al. 2020](#)). These datasets were released in March 2020, and contain observations of 300 pulsars taken between January 2014 and August 2019. To date, 12 glitches across seven pulsars have been detected as part of this timing programme using traditional methods ([Lower et al. 2020](#)). In this paper we search for new glitches beyond those discovered to date and set upper limits on the size of undetected glitches in 282 of the 300 pulsars. The layout of the paper is as follows. In Section 2 we briefly describe the data. In Section 3 we describe the HMM and explain how to choose the HMM’s control variables and search parameters. In Section 4 we present the results of the search. We narrow down the initial list of glitch detections through a veto procedure, and follow up the survivors with a refined HMM analysis to determine the basic glitch parameters: glitch epoch and glitch size. Finally in Section 5 we present systematic upper limits on the size of undetected glitches in the UTMOST data release.

2 DATA

The UTMOST pulsar timing programme is an ongoing campaign conducted at the Molonglo Observatory Synthesis Telescope, a pair of 778 m long east-west cylindrical paraboloid reflectors located near Canberra, Australia ([Bailes et al. 2017](#)). We searched a subset of the data from the first public release² ([Lower et al. 2020](#)). The data consist of times of arrival (ToAs) for 300 pulsars, mostly recorded between October 2015 and August 2019, as well as best-fit timing models. We search for glitches only in the 283 pulsars

Table 1. Observational statistics for the first UTMOST public data release. All quantities are calculated on a per-pulsar basis, and we take the minimum, mean and maximum over the complete set of pulsars in the data release.

	Minimum	Mean	Maximum
Observing timespan (d)	268	1054	2024
Cadence (d)	1.4	16	49
Number of ToAs	25	107	1458

that are not in binary systems, due to difficulties in extracting ToAs from TEMPO2 which are referenced to the reference frame of the pulsar, rather than the solar system barycentre.

The volume and density of available timing data vary significantly between pulsars. Table 1 summarises the variation in observing timespan, cadence, and number of ToAs available across the population of UTMOST pulsars. The observing timespan is the time between the first available ToA and the last available ToA for each object, and the cadence is the mean time elapsed between consecutive ToAs. A full description of the observation, data reduction and timing analysis procedures is given by [Jankowski et al. \(2019\)](#).

3 HIDDEN MARKOV MODEL

The implementation of a HMM used to search for glitches is described in detail by [Melatos et al. \(2020\)](#). Here we provide a brief description of the most pertinent aspects. Section 3.1 discusses the probabilities which determine the dynamics of the HMM, and its connection to the observed data. Section 3.2 introduces the Bayesian model selection procedure which is used to select between models with and without glitches present. In Section 3.3 we discuss the boundaries and discretisation of the state space of the HMM. The choices for the various parameters are summarised in Table 2. These are the choices used in the initial searches for previously unknown glitches (Section 4) and in setting upper limits on the sizes of undetected glitches (Section 5). Analyses aimed at estimating parameters of detected glitches (Sections 4.1–4.5) may require different parameter choices on a case-by-case basis, usually in the allowed range of frequencies, which may need to be extended by more than an order of magnitude to accommodate the glitch.

3.1 Transition and emission probabilities

A HMM is an automaton which transitions stochastically between a set of hidden states at discrete times t_1, \dots, t_{N_T} , which are spaced unequally in general. The states are hidden in the sense that they cannot be observed directly; the state of the system must be inferred from observations of auxiliary variables related probabilistically to the hidden states rather than the hidden states themselves. The probability of jumping from state q_i at time t_n to state q_j at t_{n+1} , which is called the transition probability $A_{q_j q_i}(t_n)$, depends only on the state at t_n by the Markov property. The probability that the system occupies the state q_i at time t_n , given an observational datum $o(t_n)$ collected at the same time, is called the emission probability $L_{o(t_n) q_i}$. The prior, Π_{q_i} , is the proba-

¹ https://github.com/ldunn/glitch_hmm

² <https://github.com/Molonglo/TimingDataRelease1/>

Table 2. Domain of interest of physical parameters and HMM control parameters.

Parameter	Symbol	Units	Value
Timing model reference epoch	T_0	MJD	From UTMOST
Secular frequency	f_{LS}	Hz	From UTMOST
Secular frequency derivative	\dot{f}_{LS}	Hz s ⁻¹	From UTMOST
Frequency deviation	$[f_-, f_+]$	Hz	$[-3, 3] \times 10^{-7}$
Frequency derivative deviation	$[\dot{f}_-, \dot{f}_+]$	Hz s ⁻¹	$[\max(0.1\dot{f}_{\text{LS}}, -10^{-14}), \min(-0.1\dot{f}_{\text{LS}}, 10^{-14})]$
Frequency bin size	η_f	Hz	4.0×10^{-10}
Frequency derivative bin size	$\eta_{\dot{f}}$	Hz s ⁻¹	$(\dot{f}_+ - \dot{f}_-)/11$
Timing noise strength	σ	Hz s ^{-3/2}	$\max(10^{-21}, \eta_{\dot{f}}\langle x_n \rangle^{-1/2})$
ToA uncertainty	σ_{ToA}	s	From UTMOST
Bayes factor threshold	K_{th}	None	$10^{1/2}$

bility that the system is initialized in the state q_i . Together, $A_{q_j q_i}(t_n)$, $L_{o(t_n)q_i}$, and Π_{q_i} define a HMM uniquely.

To apply a HMM to pulsar timing, we identify the hidden states q_i with a discrete grid of (f, \dot{f}) pairs, which encode the instantaneous spin frequency and its first time derivative. The hidden (f, \dot{f}) states are combined with fixed secular values f_{LS} and \dot{f}_{LS} measured at a reference epoch T_0 to give the instantaneous spin frequency $[f_{\text{LS}} + \dot{f}_{\text{LS}}(t_n - T_0)] + f$ and time derivative $\dot{f}_{\text{LS}} + \dot{f}$ respectively at time t_n . In this work we measure f_{LS} and \dot{f}_{LS} using TEMPO2 (Hobbs et al. 2006). We note that while the HMM requires a measurement of f_{LS} and \dot{f}_{LS} , these values may be derived only from a small subsection of the data in cases where a phase-connected solution spanning the whole dataset is not available. Although phase-connected solutions are available for all of the UTMOST pulsars searched in this work, the HMM does not incorporate the provided pulse numbering information. The states can be enlarged to include the second time derivative \ddot{f} (and higher derivatives), but systematic validation tests with real and synthetic data indicate that state enlargement is unnecessary for the application in this paper (Melatos et al. 2020). The observational datum at each time t_n is the ToA difference $o(t_n) = t_n - t_{n-1}$ [for ease of notation we write $x_n \equiv o(t_n)$ in the remainder of this paper], which is related probabilistically to the hidden states. The prior is deliberately chosen to be flat, i.e. Π_{q_i} is constant within a restricted parameter domain (see Section 3.3), as $q_i(t_1)$ is unknown and astrophysically irrelevant. Other structures for the HMM are possible, of course, and the reader interested in pulsar timing is encouraged to experiment with them (Rabiner 1989).

In the HMM framework, the probability of observing a particular ToA gap x_n if the hidden state of the pulsar is (f, \dot{f}) depends on the accumulated rotational phase over the gap, $\Phi(t_n; f, f_{\text{LS}}, \dot{f}, \dot{f}_{\text{LS}}, T_0)$ [denoted $\Phi(t_n; \dots)$ for brevity]. Note that $\Phi(t_n; \dots)$ satisfies $0 \leq \Phi(t_n; \dots) \leq 1$ over one period, i.e. it is in units of cycles, not radians. The full expression for $\Phi(t_n; \dots)$ is

$$\Phi(t_n; \dots) = [f + f_{\text{LS}} + \dot{f}_{\text{LS}}(t_n - T_0)]x_n - \frac{1}{2}(\dot{f}_{\text{LS}} + \dot{f})x_n^2. \quad (1)$$

The minus sign in the second term arises because we are employing a *backwards* Taylor expansion. Equation (1) can be generalised to include a secular second frequency derivative \ddot{f}_0 , if required (Melatos et al. 2020).

If $\Phi(t_n; \dots)$ is close to an integer, the probability of observing the ToA gap x_n is high. This is quantified via a

von Mises distribution, in which the probability of observing z given a hidden state (f, \dot{f}) is given by

$$L_{x_n q_i} = \frac{\exp\{\kappa \cos[2\pi\Phi(t_n; \dots)]\}}{2\pi I_0(\kappa)}, \quad (2)$$

where $I_0(x)$ is the zeroth modified Bessel function of the first kind, and κ is a parameter known as the concentration. Roughly speaking κ can be thought of as the reciprocal of the variance of $2\pi\Phi(t_n; \dots)$. There are two main contributions to variance in $\Phi(t_n; \dots)$: measurement uncertainty in the ToAs, and the spacing in the discretized f - \dot{f} grid. If the uncertainties in the ToAs at the beginning and end of the gap are $\sigma_{\text{ToA},1}$ and $\sigma_{\text{ToA},2}$ respectively then the contribution to the phase variance is $f_{\text{LS}}^2 (\sigma_{\text{ToA},1}^2 + \sigma_{\text{ToA},2}^2)$. Given spacings in f and \dot{f} of η_f and $\eta_{\dot{f}}$, the respective contributions to the phase variance are $(\eta_f x_n)^2$ and $(\eta_{\dot{f}} x_n^2/2)^2$. Combining these contributions in quadrature, we arrive at³

$$\kappa = (2\pi)^{-2} [f_{\text{LS}}^2 (\sigma_{\text{ToA},1}^2 + \sigma_{\text{ToA},2}^2) + (\eta_f x_n)^2 + (\eta_{\dot{f}} x_n^2/2)^2]^{-1}. \quad (3)$$

During each gap between consecutive ToAs, we assume that the pulsar's hidden state evolves stochastically due to timing noise in the absence of a glitch. The form of the timing noise determines the transition probability $A_{q_j q_i}$ and is unknown a priori for any individual pulsar. One reasonable model, introduced by Melatos et al. (2020) and tested satisfactorily on real data (Melatos et al. 2020; Lower et al. 2021) but certainly not unique, assumes that the timing noise is driven by a white-noise torque derivative,

$$\frac{d^2 f}{dt^2} = \xi(t), \quad (4)$$

where $\xi(t)$ is a Langevin term satisfying

$$\langle \xi(t)\xi(t') \rangle = \sigma^2 \delta(t - t') \quad (5)$$

and σ is the parameter which controls the strength of the timing noise. Equations (4) and (5) lead to a robust HMM with easy-to-specify transition probabilities $A_{q_j q_i}(t_n)$. An explicit expression for $A_{q_j q_i}(t_n)$ is given in equations 10–13 and B7–B11 of Melatos et al. (2020). The choice of (4) and (5) is pragmatic. Pulsars are not expected to obey (4) and (5) exactly for many reasons. For example, (4) and (5)

³ The factor $(2\pi)^{-2}$ in (3) was omitted accidentally by Melatos et al. (2020) in equations (8) and (C3) of the latter reference.

produce Brownian motion in the torque, whereas there is observational evidence that some pulsars exhibit Brownian motion in the frequency, i.e. $df/dt = \xi(t)$ (Cordes & Helfand 1980; Cordes & Downs 1985; Parthasarathy et al. 2019).

The choice of σ is also pragmatic and certainly not unique. A detailed study of how to optimize σ on a pulsar basis within the HMM framework is beyond the scope of this work; a first pass at some rules of thumb is found in Melatos et al. (2020). Here we follow Melatos et al. (2020) in adopting a simple prescription which is based on the fact that the HMM only tracks \dot{f} to a certain resolution, $\eta_{\dot{f}}$ (see Section 3.3). We demand that the necessary ‘‘correction’’ due to binning in the evolution of f across a ToA gap of length x_n is smaller than the dispersion in f caused by the random walk described in (4) and (5), which implies

$$\sigma = \eta_{\dot{f}} \langle x_n \rangle^{-1/2}, \quad (6)$$

where $\langle x_n \rangle$ is the average length of ToA gaps per pulsar. This ensures that the discretisation of \dot{f} does not lead to false alarms, although in some cases it may degrade the performance of the glitch detector by inflating needlessly the strength of timing noise included in the model. Any degradation in sensitivity due to this effect is reflected in the upper limits calculated in Section 5. Because the effect of discretisation of \dot{f} is absorbed into the timing noise in the model, we do not expect a significant effect on inferences made on the value of f (e.g. the pointwise most likely sequences $\hat{f}(t_n)$ discussed in Section 4). The mathematical form of (6) is justified in Section 6.1 of Melatos et al. (2020). We additionally follow Melatos et al. (2020) and impose a lower bound $\sigma \geq 10^{-21} \text{ Hz s}^{-3/2}$ to avoid numerical underflow. The prescription described here and listed in Table 2 has been successfully tested on synthetic and real data which explicitly does not conform to the timing noise model of equations (4) and (5) (Melatos et al. 2020; Lower et al. 2021).

If the model includes a glitch during a given ToA gap, then the evolution of the hidden state must be modified accordingly. We adopt the unrestrictive prescription of Melatos et al. (2020): a glitch consists of a positive frequency increment and a possible change in frequency derivative which is allowed to be positive or negative. Explicitly, if the pulsar is in the hidden state (f, \dot{f}) at the beginning of a ToA gap of length x_n , then it is allowed to transition with equal probability to any state (f', \dot{f}') as long as one has $f' > f + \dot{f}x_n$. No restriction is placed on the value of \dot{f}' (within the boundaries specified in Section 3.3).

3.2 Model selection

A HMM is a Bayesian inference tool. It works with the fundamental quantity

$$\Pr(Q_{1:N_T} | O_{1:N_T}) = \prod_{q(t_1)} L_{o(t_1)q(t_1)} \times \prod_{n=2}^{N_T} A_{q(t_n)q(t_{n-1})} L_{o(t_n)q(t_n)}, \quad (7)$$

which is the probability that the system occupies the hidden state sequence $Q_{1:N_T} = \{q(t_1), \dots, q(t_{N_T})\}$ given the observation sequence $O_{1:N_T} = \{o(t_1), \dots, o(t_{N_T})\}$ and a model $M = \{A_{q_j q_i}, L_{o(t_n)q_i}, \Pi_{q_i}\}$. The model with no glitch is denoted M_0 , and the model with a glitch during the k th ToA gap is denoted $M_1(k)$. For a given model M and timing data

$D = O_{1:N_T}$ we calculate the model evidence $\Pr(D | M)$ using the HMM forward algorithm (Rabiner 1989). We can then calculate the ratios

$$K_1(k) = \frac{\Pr[D | M_1(k)]}{\Pr[D | M_0]}, \quad (8)$$

for $1 \leq k \leq N_T$, which are Bayes factors, indicating support for each of the N_T glitch-containing models over the no-glitch model. According to Bayes’s theorem, the ratio of posterior probabilities of the two models includes an extra factor containing the prior probabilities,

$$\frac{\Pr[M_1(k) | D]}{\Pr[M_0 | D]} = \frac{\Pr[D | M_1(k)]}{\Pr[D | M_0]} \frac{\Pr(M_0)}{\Pr[M_1(k)]}. \quad (9)$$

Here we make the simplifying assumption $\Pr[M_1(k)] = \Pr(M_0)$ for all k , and so the Bayes factor $K_1(k)$ and the ratio of posterior probabilities coincide. If $\max_{1 \leq k \leq N_T} K_1(k)$ exceeds a pre-defined threshold K_{th} , we say that we have a glitch candidate. We note briefly that the permissive glitch model used may also accommodate possible abrupt changes in spin-down state (Lyne et al. 2010), and thus model selection may produce glitch candidates associated with these events as well as more typical glitch events.

To account for possible multiple glitches in a dataset, we adopt the greedy hierarchical approach described in Section 4.2 of Melatos et al. (2020). If a glitch candidate is detected when comparing the models $M_1(k)$ to M_0 , we set $k_1^* = \text{argmax}_k K_1(k)$, and then calculate the ratios

$$K_2(k_2) = \frac{\Pr[D | M_2(k_1^*, k_2)]}{\Pr[D | M_1(k_1^*)]}, \quad (10)$$

where $M_2(k_1^*, k_2)$ is the model containing two glitches at the k_1^* and k_2 th ToA gaps. If a second glitch candidate is detected, i.e. $\max_{1 \leq k_2 \leq N_T} K_2(k_2) > K_{\text{th}}$, we repeat the procedure, now comparing $M_3(k_1^*, k_2^*, k_3)$ against $M_2(k_1^*, k_2^*)$. The procedure repeats until none of the Bayes factors exceeds K_{th} .

In order to follow up each candidate, we calculate the posterior distribution of frequency and frequency derivative states during each ToA gap using the HMM forward-backward algorithm (Rabiner 1989). The logic behind this step is discussed in detail in Section 4.3 and Appendix A of Melatos et al. (2020). This posterior distribution can then be used to infer the sequence of most likely frequency states, and hence the most likely size of the frequency jump due to the glitch.

The Bayes factor threshold determines when we have a glitch candidate to be followed up with further analysis. Here we adopt a fixed threshold of $10^{1/2}$, motivated by the synthetic data tests presented in Section 6 of Melatos et al. (2020). $K_{\text{th}} = 10^{1/2}$ gives a false alarm probability of roughly 1%, provided that the timing noise is not much stronger than what is included in the HMM.

3.3 Domain of interest

The domain of interest (DOI) refers to the set of hidden states which are included in the HMM. As in Melatos et al. (2020), we consider only DOIs which form a grid in a ‘‘reasonable’’ f - \dot{f} region, which is restricted to avoid wasteful computation; the state sequence $Q_{1:N_T}$ cannot wander unreasonably far from the TEMPO2 fit f_{LS} and \dot{f}_{LS} , because

timing noise and glitches represent modest perturbations on the secular trend. The choices to be made are then the boundaries of the region, and the spacing between points in the grid. The typical DOI parameters used in this work are summarised in Table 2.

When searching for unknown glitches and setting upper limits on the size of undetected glitches, the boundary of the f region is chosen to be the same for all pulsars in this study: the region covered is $-3 \leq f / (10^{-7} \text{ Hz}) \leq 3$. This range generously brackets the typical wandering due to timing noise measured in young pulsars to date. The spacing in f is also held fixed for all pulsars at $\eta_f = 4 \times 10^{-10} \text{ Hz}$. This choice represents a trade-off between sensitivity and computational cost. When performing follow-up analysis of a glitch candidate, the range and spacing in f are sometimes modified to encompass the pre- and post-glitch frequencies. In the case of a large glitch, this means increasing the upper boundary of the f region to a value on the order of 10^{-5} Hz . In this case the value of η_f must also be increased to keep the total number of hidden states in the DOI small enough that the computation remains tractable.

The domain of interest and grid spacing in \hat{f} vary between pulsars when searching for new glitches and setting upper limits. Given a measured secular spindown \dot{f}_{LS} , we take the \hat{f} region to be $|\hat{f}| \leq \min(10^{-14} \text{ Hz s}^{-1}, -0.1\dot{f}_{\text{LS}})$. The region is empirically determined, guided by validation experiments with synthetic data, which show that timing-noise-driven excursions in \hat{f} are small compared to \dot{f}_{LS} (Melatos et al. 2020). The \hat{f} spacing $\eta_{\hat{f}}$ is chosen so that there are always 11 points in the domain. This choice is motivated principally by a desire to keep computational cost under control. As a side effect, pulsars with larger values of \dot{f}_{LS} have larger values of σ in the HMM’s timing noise model: a larger \dot{f}_{LS} gives a larger $\eta_{\hat{f}}$, and by equation (6) this in turn gives a larger σ . While this relation between \dot{f}_{LS} and σ comports with the astrophysical fact that timing activity is correlated with \dot{f}_{LS} (Arzoumanian et al. 1994; Hobbs et al. 2010; Lower et al. 2020), it does not do so by design. It is a consequence of pragmatic choices which aim to keep false alarms rare [in the case of equation (6)] and computational cost low (in the case of the choice of $\eta_{\hat{f}}$).

4 UTMOST GLITCHES

We search for glitches in the UTMOST timing data in three stages. In the initial stage, every pulsar is analysed using the HMM parameters set out in Table 2. The results of the initial search are presented in Table 3. We report every glitch candidate with a Bayes factor greater than $K_{\text{th}} = 10^{1/2}$. In the second stage, candidates are followed up with a simple veto procedure, and an estimates of the glitch parameters are calculated for those candidates which survive the veto.

Before estimating the parameters of each candidate, we check that the candidate is not due to a transient disturbance. Such a disturbance may be caused by the conditions at the observatory, e.g. a clock error (Verbiest & Shaifullah 2018). It may also have astrophysical origins. Some pulsars exhibit “mode-changing”, switching between a small number of distinct pulse profiles on timescales of minutes, which can lead to apparent jumps in the pulse phase (Backer 1970;

Helfand et al. 1975; Wang et al. 2007). Changes in propagation through the interstellar medium can also lead to similar apparent phase jumps (Goncharov et al. 2021). To exclude events of this kind, we re-run the HMM for each candidate using identical parameter choices, but with the ToAs immediately bracketing the candidate removed. If one then obtains $K_1(k) < K_{\text{th}}$, the candidate is vetoed and no further analysis is performed. The results of this veto procedure are noted in the right-most column of Table 3. Three candidates are vetoed in this way, leaving eight to be followed up in the second stage of the search. This veto procedure does risk discarding candidates which correspond to true glitches, if the cadence around the candidate is low and the glitch is small. Appendix A describes further investigation of each of the three vetoed candidates, in an effort to determine whether they are transient disturbances caused by one of the factors above.

The second stage of the search entails estimating the parameters of each candidate based on the sequence of most likely hidden states (Melatos et al. 2020), which gives the evolution of f , from which the approximate epoch and glitch size can be read off. The follow-up analyses are performed first within an f range which is wider than the range used in the initial analysis. For all seven veto survivors which are ultimately identified as genuine glitch events (i.e. all but the candidate in J1622–4950, see Section 4.3), the maximum allowed frequency deviation is $2.5 \times 10^{-5} \text{ Hz}$ rather than $3 \times 10^{-7} \text{ Hz}$, so that large glitches are characterised more accurately. The extended f range degrades the sensitivity of the HMM to small glitches, as η_f must increase to keep the computation tractable, which is why a smaller f range is tested in the first stage. After the analysis with an extended f range is complete, each dataset is divided into pre- and post-glitch sections, and these sections are searched again with the smaller f range and η_f used in the initial search. No additional glitch candidates are detected in this way.

The parameter estimation results are summarised in Table 4. Two outputs are of particular interest: the sequences of most likely frequency states⁴ $\hat{f}(t_n)$, and the posterior distribution $\gamma_f(t_n)$ of $f(t_n)$. The most likely frequency states are obtained as the modes of the posterior distribution of states q_i at each timestep t_n , where the posterior is denoted $\gamma_{q_i}(t_n)$ [defined in equation A13 of Melatos et al. (2020)]. The posterior frequency distribution $\gamma_f(t_n)$ is obtained by marginalising $\gamma_{q_i}(t_n)$ over \hat{f} . Plots of $\hat{f}(t_n)$ and $\ln \gamma_f(t_n)$ for the follow-up analyses are shown in Figs. C1–C8.

We can obtain the posterior frequency derivative distribution in much the same way. We do not present these distributions here, as coarse discretisation of \hat{f} in the DOI often leads to unconstraining \hat{f} posteriors. An example is shown in Fig. C9, showing $\gamma_{\hat{f}}(t_n)$ from the follow-up analysis of J1731–4744 described in Section 4. The posterior has support over a significant fraction of the DOI, particularly after the glitch at the 103rd ToA gap, which makes it difficult to draw meaningful conclusions about the evolution of \hat{f} across the glitch.

⁴ The point-wise estimate $\hat{f}(t_n)$ is the most likely value of f at t_n given the data $O_{1:N_T}$. This is subtly different from the f component of the n th element of the most likely sequence of hidden states.

Table 3. Properties of the initial glitch candidates detected in the first UTMOST data release.

Object	Epoch MJD	$\ln K_1(k)$	Vetoed? Y/N
J0742–2822	57527 ± 2	4.05	Y
J0835–4510	58218 ± 4	4.7×10^4	N
J1105–6107	57417 ± 4	1.27	Y
J1257–1027	58651 ± 10	5.4	N
J1359–6038	58189 ± 2	11.7	Y
J1452–6036	58638 ± 1	126	N
J1622–4950	58076 ± 8	8.46	N
J1703–4851	58543 ± 21	47.5	N
J1709–4429	58222 ± 6	1.17×10^3	N
J1731–4744	58007 ± 2	1.20×10^5	N
J1740–3015	58393 ± 5	4.47×10^4	N

Table 4. Properties of the detected glitches confirmed by follow-up analyses. The fractional glitch sizes recovered in the HMM analysis are denoted by $\Delta f/f$, while the values reported by Lower et al. (2020) are denoted by $(\Delta f/f)_{\text{lit.}}$. Phase ambiguity due to periodic observational scheduling prevents inferring $\Delta f/f$ for PSR J1452–6036 (see Section 4.2).

Object	Epoch MJD	$\Delta f/f$ $\times 10^{-9}$	log Bayes factor	$(\Delta f/f)_{\text{lit.}}$ $\times 10^{-9}$
J0835-4510	57732 ± 4	1436 ± 3	7.43×10^4	$1448^{+0.9}_{-0.8}$
	58521 ± 7	2467 ± 13	3.36×10^3	$2501.2^{+2.6}_{-3.2}$
J1257–1027	58650 ± 16	2.2 ± 0.4	16.4	$3.20^{+0.16}_{-0.57}$
J1452–6036	58606 ± 3	–	1.40×10^3	$270.7^{+0.3}_{-0.4}$
J1703–4851	58543 ± 21	10 ± 2	47.5	$19.0^{+1.0}_{-0.7}$
J1709–4429	58200 ± 27	2405 ± 3	220	54.6 ± 1.0
J1731–4744	58007 ± 2	3150 ± 14	1.40×10^5	$3149^{+0.5}_{-0.4}$
J1740–3015	57476 ± 17	225 ± 14	1.43×10^3	$237.7^{+13.2}_{-9.3}$
	58240 ± 11	829 ± 14	9.37×10^3	$842.3^{+7.1}_{-5.6}$

We remind the reader that the phase model of the HMM is not the same as the phase model of TEMPO2. The HMM allows inter-glitch wandering of f and \dot{f} , and transitions between the hidden f - \dot{f} states occur only at the start of ToA gaps. In addition, the HMM includes no explicit modelling of quasi-exponential post-glitch recovery processes. For all of these reasons, we expect modest discrepancies between the glitch parameters estimated using the HMM and those reported by previous authors, who use TEMPO2 and TEMPO-EST to measure the glitch parameters. Those glitches which merit additional discussion are covered in the remainder of this section.

4.1 PSR J0835-4510

PSR J0835-4510 (Vela) exhibits frequent large glitches, at a rate of roughly one every three years with $\Delta f/f \sim 10^{-6}$ typically (Howitt et al. 2018). The UTMOST data available for this pulsar consist of 1420 ToAs recorded between January 9 2014 and September 17 2018. To keep the analysis computationally tractable, we divide the dataset into three sections of approximately 500 ToAs each, with the sections overlapping by 50 ToAs to ensure that any glitches that occur during the gaps between sections were not missed. Details of the section boundaries can be found in Table 5. Plots of $\hat{f}(t_n)$ and $\ln \gamma_f(t_n)$ for the three sections are shown in Fig. C1.

We detected two large glitches in the data, both of which have been reported previously (Palfreyman 2016; Sarkissian

Table 5. Data segmentation in the PSR J0835–4510 analysis.

Section	Start MJD	End MJD
1	56666	56898
2	56868	57606
3	57552	58692

et al. 2019). The first, detected between MJD 57728 and MJD 57734, has $\Delta f/f = (1436 \pm 3) \times 10^{-9}$. The second, detected between MJD 58514 and MJD 58529, has $\Delta f/f = (2467 \pm 13) \times 10^{-9}$. We note a feature which recurs several times throughout these analyses: $\gamma_f(t_n)$ shows multiple peaks for the timesteps following the second glitch, indicating the existence of multiple glitch models which describe the data well, despite being widely separated in frequency. One can see this clearly in the bottom right panel for Fig. C1, where the yellow contour splits into three branches for ToA index ≥ 533 . Dunn et al. (2021) showed that this effect is due to periodicity in the observation schedule. If the separations between consecutive ToAs are nearly integer multiples of a common period T , there can be a degeneracy between glitch models with Δf differing by $1/T$. Since mid-2017 the Molonglo Observatory Synthesis Telescope has operated as a transit instrument (Venkatraman Krishnan et al. 2020), so each pulsar is observed at roughly the same local sidereal time for every observation. Hence, to a good approximation,

ToAs recorded by UTMOST after mid-2017 per pulsar are separated by integer numbers of sidereal days. Indeed, the spacing between the peaks in $\gamma_f(t_n)$ in Fig. C1 is close to $1/(1 \text{ sidereal day}) = 1.1606 \times 10^{-5} \text{ Hz}$.

The degeneracy between glitch models may be alleviated by additional observations which disrupt the periodic scheduling. Fortunately, PSR J0835–4510 is an extremely well-studied pulsar, and the second glitch in the UTMOST dataset has been independently reported by several other facilities (Sarkissian et al. 2019; Kerr 2019; Gancio et al. 2020). Kerr (2019) estimated the size of the glitch to be $\Delta f/f = (2491.1 \pm 0.5) \times 10^{-9}$ based on data from the *Fermi* Large Area Telescope (Atwood et al. 2009), and Gancio et al. (2020) estimated the size of the glitch to be $\Delta f/f = 2682 \times 10^{-9}$ based on observations taken at the Argentine Institute of Radio Astronomy. These measurements are consistent with the HMM estimate, and with the estimate given by Lower et al. (2020).

4.2 PSR J1452–6036

We detected one glitch in this pulsar, occurring between MJD 58603.6 and MJD 58604.6. The log Bayes factor over the no-glitch model is 1.4×10^3 .

Plots of $\hat{f}(t_n)$ and $\ln \gamma_f(t_n)$ are shown in Fig. C3. Inspection of $\gamma_f(t_n)$ indicates that caution is warranted when determining Δf for this glitch. The inferred $\hat{f}(t_n)$ shown in the left panel of Fig. C3 suggests a glitch size of $\Delta f/f = 3869 \times 10^{-9}$. However, as with PSR J0835–4510, the three peaks in $\gamma_f(t_n)$ indicate the existence of multiple glitch models which are widely separated in Δf (the separation between peaks is approximately $1.1605 \times 10^{-5} \text{ Hz}$) but nevertheless describe the available data well. This glitch was previously reported by Lower et al. (2020) as occurring at MJD 58600.29(5) with $\Delta f/f = 270.7_{-0.4}^{+0.3}$. Using the data in the UTMOST public data release, Dunn et al. (2021) demonstrated that the available data are consistent with $\Delta f/f = 270 \times 10^{-9} + N/(fT)$ with $N = 0, 1, 2$ and $T \approx 1$ sidereal day, thereby including the Lower et al. (2020) value as one possible option (with $N = 0$). This result is in good agreement with the HMM analysis: the three peaks in the post-glitch frequency posterior generated by the HMM lie at $\Delta f/f = 269 \times 10^{-9}$, 2070×10^{-9} , and 3869×10^{-9} . Fortunately, independent observations at the Parkes radio telescope constrain the size of the glitch well, with Jankowski et al. (2021) measuring $\Delta f/f = 270.52(3) \times 10^{-9}$. This value is consistent with the Lower et al. (2020) estimate and the smallest peak in $\gamma_f(t_n)$. Note that we do not expect the tallest peak in the post-glitch frequency posterior to always correspond to the true glitch size when confounded by periodic scheduling (Dunn et al. 2021).

4.3 PSR J1622–4950

PSR J1622–4950 is a special object: it is a magnetar which shows large torque variations, with much larger variations in \dot{f} than the DOI $\dot{f}_{\text{LS}} \pm 1 \times 10^{-14} \text{ Hz s}^{-1}$ allowed in the initial search for glitches (Camilo et al. 2018). While this glitch candidate is not vetoed by removing ToAs either side of the glitch, it is probably an artifact caused by the first-pass DOI being too restrictive. We note that the sequences

of most likely f and \dot{f} states using the initial search parameters run up against the edges of the DOI. We re-analyse the dataset using a DOI which is somewhat expanded in both f and \dot{f} , with boundaries in f at $f_{\text{LS}} \pm 5 \times 10^{-6} \text{ Hz}$ and boundaries in \dot{f} at $\dot{f}_{\text{LS}} \pm 1 \times 10^{-12} \text{ Hz s}^{-1}$, searching for any glitch candidates in exactly the same way as before. No glitch candidate is detected in this reanalysis, so we do not consider this candidate further. For completeness, Figure C4 shows the sequence of most likely frequencies and the posterior frequency probability for the re-analysis with the extended DOI. The posterior has a relatively complex structure, because both the timing noise included in the HMM and the errors on individual TOAs are large, giving the HMM significant freedom in finding viable sequences of hidden states. The large torque variations in PSR J1622–4950 make it difficult (though not impossible) to obtain a phase-connected timing solution covering timespans longer than a few months (Levin et al. 2010). We note briefly that the HMM offers a straightforward method of obtaining the pulse numbering and hence a phase-connected solution: from the sequence of most likely frequencies $\hat{f}(t_n)$ and frequency derivatives $\dot{\hat{f}}(t_n)$ it is easy to calculate the number of pulses during each gap via equation (1). From this information the relative pulse numbering is easily derived, and a phase-connected solution obtained.

4.4 PSR J1709–4429

We measured a glitch in this pulsar during the ToA gap between MJD 58172.9 and MJD 58227.7, with size $\Delta f/f = (2405 \pm 3) \times 10^{-9}$. The log Bayes factor over the no-glitch model is 220.

Plots of $\hat{f}(t_n)$ and $\ln \gamma_f(t_n)$ are shown in Fig. C6. This detection corresponds to a glitch which was previously reported as occurring at MJD 58178 \pm 6 with a glitch size of $\Delta f/f = 54.6 \pm 1.0 \times 10^{-9}$ (Lower et al. 2018, 2020). The glitch reported previously is smaller than the one we recover in this analysis. As with the glitches in PSR J0835–4510 and PSR J1452–6036, the post-glitch frequency posterior is multiply peaked, with peaks separated by $\sim 1/(1 \text{ sidereal day})$ due to periodic observation scheduling. Dunn et al. (2021) found that a combined dataset incorporating both the UTMOST data release and observations taken at the Parkes Observatory is consistent with $\Delta f/f = (2432 \pm 0.1) \times 10^{-9}$. Hence we expect that the glitch size recovered by the HMM reflects the true glitch properties.

4.5 PSR J1740–3015

In the follow-up analysis of PSR J1740–3015 we detected two glitches. One glitch occurs in the ToA gap between MJD 57459 and MJD 57486, with size $\Delta f/f = (225 \pm 14) \times 10^{-9}$, and is detected with a log Bayes factor of 1.43×10^3 . The second glitch occurs in the ToA gap between MJD 58229 and MJD 58243, with size $\Delta f/f = (829 \pm 14) \times 10^{-9}$, and is detected with a log Bayes factor of 9.37×10^3 . Plots of $\hat{f}(t_n)$ and $\ln \gamma_f(t_n)$ are shown in Fig. C8.

The first glitch was initially reported by Jankowski et al. (2016) based on UTMOST data. They reported $\Delta f/f = (227.29 \pm 0.03) \times 10^{-9}$, consistent with the HMM estimate. Multiple peaks are visible in $\gamma_f(t_n)$ after the second glitch.

However, this second glitch was also reported by [Basu et al. \(2020\)](#) based on data taken at the upgraded Giant Metrewave Telescope; they reported $\Delta f/f = 837.4(2) \times 10^{-9}$, consistent with the HMM analysis. No post-glitch recovery term was included in their fit.

Two additional glitches have been reported in this pulsar during the timespan covered by the UTMOST first public release, occurring at $\text{MJD } 57296.5 \pm 0.9$ and $\text{MJD } 57346.0 \pm 0.6$ with sizes $\Delta f/f = 1.30 \pm 0.04 \times 10^{-9}$ and $\Delta f/f = 1.94 \pm 0.02 \times 10^{-9}$ respectively ([Jankowski et al. 2015, 2016](#)). We do not detect these glitches in our analysis. This is not surprising, as the 90% upper limit listed in [Table 6](#), namely $\Delta f^{90\%}/f = 41 \times 10^{-9}$ (see [Section 5](#)), is an order of magnitude larger than the reported sizes of the undetected glitches.

5 SIZE UPPER LIMITS

Having detected nine glitches among seven pulsars out of the 283 pulsars searched, we now turn to the question of completeness of this glitch sample. In [Section 5.1](#) we discuss the 90% frequentist upper limits set on 282 UTMOST pulsars, which are the main result of this section⁵. In [Section 5.2](#) we compare these upper limits to the observed population of glitches, and discuss the completeness of the sample of glitches reported in this work. Finally in [Section 5.3](#) we investigate how much quasi-exponential glitch recovery affects the upper limits of [Section 5.1](#).

5.1 Frequentist limits

In order to assess completeness, we set 90% frequentist upper limits $\Delta f^{90\%}$ on the sizes of undetected glitches for each pulsar in the UTMOST data release. The upper limit is defined, such that there is a 90% probability of detecting a glitch of size $\Delta f^{90\%}$ in the correct ToA gap, if the glitch occurs at a random epoch distributed uniformly over the entire dataset (excluding the first two and last two ToAs). In [Sections 5.1](#) and [5.2](#), for the sake of simplicity, we do not include a jump in \dot{f} at the glitch epoch or an exponential post-glitch recovery; the latter effect is considered in [Section 5.3](#). The probability of detection for a given pulsar and a given Δf is estimated with 100 synthetic datasets generated using LIBSTEMPO with a randomly chosen glitch epoch and noise injected at the level reported in the UTMOST data release. The injected noise includes both Gaussian ToA measurement error and timing noise, e.g. spin wandering intrinsic to the pulsar ([Goncharov et al. 2021](#)). The procedures for generating the synthetic datasets and estimating $\Delta f^{90\%}$ are described in [Appendix B](#). The prescription for choosing HMM parameters is identical to the prescription for real data, as laid out in [Section 3](#). A systematic upper limit injection study of this kind is practical only because the HMM runs fast and automatically without human intervention ([Melatos et al. 2020](#)).

[Figure 1](#) shows a histogram of $\Delta f^{90\%}/f$ for the 282 pulsars analysed here. The majority (96%) of the $\Delta f^{90\%}/f$

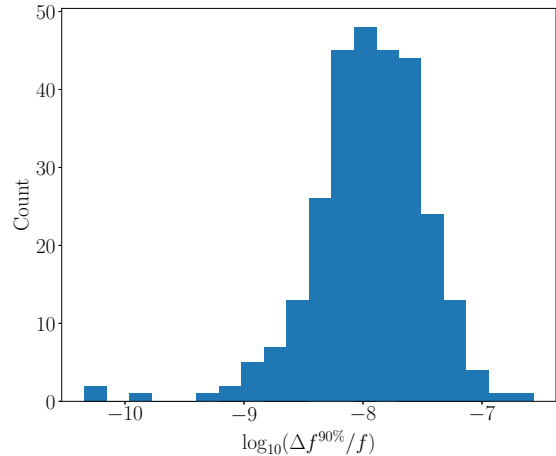


Figure 1. Histogram of 90% frequentist upper limits on fractional glitch size for the 282 UTMOST pulsars analysed in this paper.

Object	$\Delta f^{90\%}/f$ $\times 10^{-9}$
J0835–4510	6.7
J1257–1027	1.2
J1452–6036	14
J1703–4851	12
J1709–4429	12
J1731–4744	62
J1740–3015	41

Table 6. 90% frequentist upper limits on the undetected glitch size in the seven UTMOST pulsars for which at least one glitch is detected by the HMM.

values lie between 10^{-9} and 10^{-7} . The mean fractional upper limit for our sample is $\langle \Delta f^{90\%}/f \rangle = 1.9 \times 10^{-8}$. The minimum $\Delta f^{90\%}/f$ value is 4.5×10^{-11} for the millisecond pulsar PSR J1730–2304, while the maximum is 2.7×10^{-7} in the young pulsar PSR J1123–6259. We do not list every value of $\Delta f^{90\%}/f$ here for readability, but [Table 6](#) lists the values for the seven pulsars in which we report at least one glitch in [Section 4](#). A complete list of $\Delta f^{90\%}$ values can be found in the Supplementary Materials.

No upper limit is obtained for PSR J1622–4950, where strong timing noise in the HMM (see [Section 4.3](#)) and a periodic observation schedule mean that it is not possible to attain a detection probability of 90% for any plausible glitch size. Typically, even in the presence of significant timing noise one can increase Δf to a point where timing noise can no longer account for the frequency jump. However, if observations are periodic as they are here, with a period of 1 sidereal day, then glitches with sizes Δf larger than $N/(1 \text{ sidereal day})$ (where N is an integer) are recovered as glitches with size $\Delta f - N/(1 \text{ sidereal day})$. Hence they may never be detected by the HMM if the timing noise is large enough to account for a change in frequency of $\Delta f - N/(1 \text{ sidereal day})$.

For the data analysed here, the sensitivity of the HMM

⁵ We are unable to set a 90% upper limit for the magnetar PSR J1622–4950, as discussed in [Section 5.1](#).

is principally controlled by the largest observing gaps in the data. Large gaps allow for significant deviations in the spin frequency to be absorbed into the timing noise model in the HMM, with the expected fractional upper limit proportional to $\dot{f}_+ \max_n x_n$. When this effect dominates, a regular and frequent observing cadence is most useful in obtaining more stringent upper limits. However, we caution that this is not true in all regimes. When the observing cadence is short enough, or the allowed wandering due to timing noise is small enough, the sensitivity of the HMM is instead controlled by the phase uncertainty incorporated into the HMM via the κ parameter (see Section 3.1). In this case the expected fractional upper limit is roughly proportional to $2\pi\kappa^{-1/2}\langle x_n \rangle^{-1}$, and increasing the cadence (decreasing $\langle x_n \rangle$) further will give *lower* sensitivity, if κ is dominated by the contribution from σ_{ToA} , which is independent of x_n . We refer the reader to section 6 and appendix G of Melatos et al. (2020) for further discussion on the sensitivity of the HMM glitch detector.

5.2 Population-level comparison

We compare the upper limits obtained in Section 5.1 to the observed size distribution aggregated across the entire pulsar population, as recorded in the Jodrell Bank Observatory (JBO) glitch catalogue⁶ (Espinoza et al. 2011). This is not exactly a like-for-like comparison: the catalogue of observed glitches combines a wide variety of datasets and analyses, with varying observation scheduling and glitch detection strategies. Nevertheless it is instructive to ask what categories (if any) of glitches observed in other pulsars are not detectable by the HMM in the UTMOST data release.

Fig. 2 shows a histogram of all $\Delta f/f$ values listed in the JBO glitch catalogue overlaid with a histogram of the upper limits obtained in this analysis. There is a population of detected glitches in the JBO catalogue with $10^{-12} \lesssim \Delta f/f \lesssim 10^{-9}$ which are smaller than the 90% upper limits obtained for most of the pulsars in our sample. Glitches in this size range are unlikely to be detected by the search in this paper. Of course, this raises the interesting question of whether some glitches in the JBO catalogue with $\Delta f/f \lesssim 10^{-9}$ are false alarms. This comes down to distinguishing timing noise from glitches through Bayesian model selection and calculating $\Delta f^{90\%}$ for the relevant observational studies in the literature, a task which is challenging without an unsupervised algorithm like the HMM (Janssen & Stappers 2006; Chukwude & Urama 2010; Espinoza et al. 2014; Yu & Liu 2017).

By way of comparison, we briefly highlight three other investigations of glitch detectability which are similar in spirit to the current work. Janssen & Stappers (2006) performed Monte Carlo injections for a single pulsar, PSR J0358+5413, finding that glitches as small as $\Delta f/f = 10^{-11}$ can be detected by eye. It is unclear, however, how confidently such glitches can be detected. Espinoza et al. (2014) employed an automated glitch detection algorithm to search for glitches in the Crab pulsar, and reported a minimum glitch size in that case, which is intrinsic to the pulsar and not an artifact of the detector performance. This technique

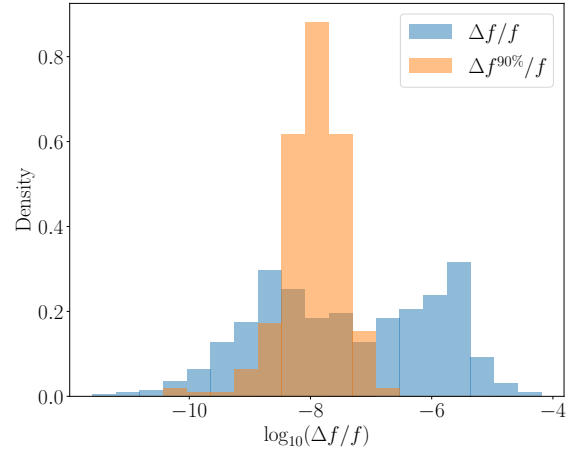


Figure 2. Histogram of size upper limits $\Delta f^{90\%}/f$ computed in Section 5.1 (orange) compared with sizes $\Delta f/f$ detected in the entire pulsar population in the Jodrell Bank Observatory catalogue (blue).

has also been applied to the Vela pulsar, and a lack of small glitches was reported in that case also (Espinoza et al. 2021). However, the detector returns a large number of (anti-)glitch candidates which must be classified after the fact as timing noise or glitches. This obstructs the characterisation of the detector in a controlled environment via a suite of synthetic data tests, as well as the application of this technique to a large number of datasets. Yu & Liu (2017) assessed the completeness of the glitch catalogue reported in Yu et al. (2013) through Monte Carlo simulations in which glitch detection was performed using TEMPO2. They concluded that the reported glitch catalogue contains all glitches detectable by manual inspection of timing residuals. However the criterion for a positive detection relies on knowing the true glitch epoch; it cannot be extended to finding previously unknown glitches. We emphasise that although some glitches may be missed, the upper limits calculated here are derived from simulated searches of every pulsar individually.

5.3 Post-glitch recovery

Many (but not all) glitches exhibit a degree of recovery over timescales of days to months, such that part (or all) of Δf reverses, leaving a permanent frequency jump Δf_p (Shemar & Lyne 1996). The recovery is typically modelled as one or more exponential terms in the post-glitch frequency evolution, viz.

$$f(t) = f(0) + \Delta f_p + \sum_{i=1}^M \Delta f_i e^{-t/\tau_i} \quad (11)$$

for a hypothetical glitch occurring at $t = 0$, where the Δf_i are the sizes of the M exponentially recovering components, with recovery timescales τ_i . In many events one has $M = 1$, but where the pulsar is well-observed following the glitch, more exponential terms may be incorporated, e.g. $M \leq 4$ (Dodson et al. 2002). The glitch population as a whole exhibits a wide variety of recovery behaviour. Values of the

⁶ <http://www.jb.man.ac.uk/pulsar/glitches/gTable.html>

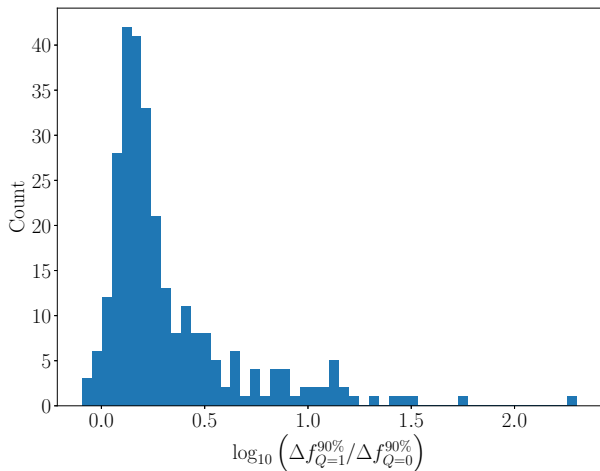


Figure 3. Histogram for 282 UTMOST pulsars of the ratio of 90% glitch size upper limit computed with a completely recovering glitch ($\Delta f_{Q=1}^{90\%}$) to the 90% upper limit computed with no recovery ($\Delta f_{Q=0}^{90\%}$).

healing parameter

$$Q = \frac{\sum_i \Delta f_i}{\Delta f_p + \sum_i \Delta f_i} \quad (12)$$

are typically between 0 and 1, with $Q \ll 1$ being more common for large glitches ($\Delta f_p/f \gtrsim 10^{-6}$) (Yu et al. 2013).

In Section 5.1 we set 90% frequentist upper limits on the sizes of undetected glitches assuming a glitch model (both in the simulated data and the HMM) with no recovery (i.e. $Q = 0$). We now investigate whether including recovery in the simulated data significantly changes these upper limits. To this end, we recompute 90% frequentist upper limits as in Section 5.1, but now assume that the glitch recovers completely (i.e. $Q = 1$ in the simulated data) on a timescale of $\tau_1 = 100$ d, typical of many pulsars (Yu et al. 2013). Note that we do not modify the phase model of the HMM in any way — no attempt is made to model the exponential recovery as part of the glitch detection step. Fig. 3 shows a histogram of the ratios between the $Q = 1$ and $Q = 0$ values of $\Delta f^{90\%}$ for each pulsar. In the majority of cases the effect of recovery is not severe: for 87% of the pulsars one obtains $\Delta f_{Q=1}^{90\%} < 5\Delta f_{Q=0}^{90\%}$. Hence we do not expect complete glitch recovery on month-long timescales to affect significantly the results presented in Section 5.1. The outliers with large ratios $\Delta f_{Q=1}^{90\%}/\Delta f_{Q=0}^{90\%}$ typically have small intrinsic \dot{f}_{LS} , with $\dot{f}_{\text{LS}} > -10^{-15} \text{ Hz s}^{-1}$. In this regime the extra \dot{f} due to quasi-exponential recovery is much larger than the range of \dot{f} in the DOI, which covers only $\pm 0.1\dot{f}_{\text{LS}}$ (see Section 3.3). Hence the HMM struggles to track the evolution of f and \dot{f} , and is correspondingly less sensitive. Conversely, for six pulsars we have $0.8 < \Delta f_{Q=1}^{90\%}/\Delta f_{Q=0}^{90\%} < 1$. In all but one case these pulsars are monitored with relatively high cadence, and have sufficiently wide ranges in the \dot{f} DOI to allow the tracking of the extra \dot{f} from the exponential recovery⁷ Hence

⁷ In the remaining case, which is PSR J1736–2457, we expect

we expect that the change in \dot{f} from the recovery allows the HMM to detect glitches more readily in this regime.

The above analysis only considers one point in the space of possible (Q, τ_1) choices (though it is a fairly typical point). A full exploration of the Q - τ_1 plane for every pulsar in the UTMOST data release is beyond the scope of this paper. We emphasise that the conclusions drawn about upper limits here and in Section 5.1 are conditional not only on the analysis method but also on the assumed glitch model, a feature of any timing analysis.

6 CONCLUSION

In this paper we present a search for glitches using a HMM in 283 pulsar timing datasets released by the UTMOST pulsar timing programme, covering observations taken between October 2015 and August 2019. We detect nine glitches among seven pulsars, all of which have been previously reported. The inferred Δf is usually consistent with previous discoveries, except when there is ambiguity due to near-periodic scheduling (Dunn et al. 2021). In this case the discrepancy in Δf can be large, viz. an integer multiple of T^{-1} , where T is the observation scheduling period. For all the glitches detected in this work, complementary observations by other observatories allow the unambiguous determination of Δf . In principle the Δf inferred from an HMM analysis may be biased by quasi-exponential post-glitch recovery, which is not included in the HMM in its current implementation. However, this effect is demonstrated to be small for the glitches measured in this work, typically $\lesssim 2\%$ for the 7 objects studied here. Incorporating post-glitch recoveries into the HMM (at the expense of introducing new parameters) is a priority for future work.

For each object, we perform injection studies to set frequentist upper limits on the size of undetected glitches. The mean 90% upper limit on the fractional size of undetected glitches is $\langle \Delta f^{90\%}/f \rangle = 1.9 \times 10^{-8}$. The smallest value of $\Delta f^{90\%}/f$ is 4.1×10^{-11} , calculated for the millisecond pulsar PSR J1730-2304. The largest value of $\Delta f^{90\%}/f$ is 2.7×10^{-7} , calculated for the young pulsar PSR J1123–6259. Obtaining more stringent upper limits using the existing data would require a more complete characterisation of the timing noise and a comprehensive understanding of how different timing noise models ought to be included in the HMM, a challenge which is faced by other glitch detection schemes (Chukwude & Urama 2010; Espinoza et al. 2014; Singha et al. 2021). Independent of these timing noise considerations, future observing campaigns can provide stricter upper limits with higher cadence and/or more sensitive observations. We show that glitch recovery has a mild effect on the upper limits; the upper limits for 87% of the objects increase by no more than a factor of 5, if it is assumed that the undetected glitch recovers completely on a fiducial time-scale of 100 d.

Understanding the completeness of glitch catalogues is

that simple statistical fluctuation is the cause: the observing cadence is relatively low, with several gaps of 10–60 days present in the data. In this case, when relaxations are included and the effect of a glitch on f and \dot{f} can decay away within one or two post-glitch ToAs, the estimated value of $\Delta f^{90\%}$ may depend somewhat on the epochs of the injected glitches in the synthetic datasets.

Table 7. Top and bottom five $-\dot{f}\langle\Delta t\rangle$ values among pulsars observed by UTMOST. The Pearson correlation coefficients between $\Delta f/f$ and the forward (r_+) and backward (r_-) waiting times are also listed. The objects in the top (bottom) half of the table are more likely to exhibit cross-correlations between glitch size and forward (backward) waiting time.

Object	N_g	$-\dot{f}\langle\Delta t\rangle$ (Hz)	r_+	r_-
J1709–4429	5	1.8×10^{-3}	0.66	–0.47
J1803–2137	6	1.4×10^{-3}	0.91	–0.24
J0835–4510	20	1.2×10^{-3}	0.24	0.55
J1048–5832	6	6.0×10^{-4}	0.58	–0.48
J1105–6107	5	4.2×10^{-4}	0.87	–0.37
J1731–4744	5	4.4×10^{-5}	–0.71	0.99
J1740–3015	36	3.5×10^{-5}	0.29	–0.02
J1705–1906	4	1.2×10^{-5}	0.97	–0.54
J1825–0935	7	1.1×10^{-5}	0.91	–0.30
J1902+0615	6	2.0×10^{-6}	0.49	–0.31

essential to falsifying models of glitching behaviour. For instance, Melatos et al. (2018) predicted (under certain weak, astrophysics-independent assumptions) that pulsars with large values of $-\dot{f}\langle\Delta t\rangle$ (where $\langle\Delta t\rangle$ is the mean waiting time between glitches) should show significant correlations between the size of a glitch and the forward waiting time to the next glitch. Similarly, pulsars with small values of $-\dot{f}\langle\Delta t\rangle$ are predicted to be the most likely to exhibit correlations between glitch size and backward waiting time, although the latter correlations are predicted to be weaker. As a foretaste of what is possible, Table 7 shows the five highest and five lowest values of $-\dot{f}\langle\Delta t\rangle$ amongst the pulsars which have been observed in the first UTMOST data release, as well as the Pearson correlation coefficients between $\Delta f/f$ and the forward and backward waiting times. While most of these pulsars do not yet have enough glitches observed for any statistically significant conclusions to be drawn, there is tentative evidence for strong forward correlations in the pulsars with the largest values of $-\dot{f}\langle\Delta t\rangle$. Continued high-cadence monitoring of these pulsars and a good understanding of the likelihood that a glitch of a given size might not have been detected are essential to falsifying the proposed relations. Improved understanding of the completeness of glitch catalogues is also important to studies of the physical conditions involved. Several authors have investigated the nature of the neutron superfluid in the inner crust by studying glitching behaviour (e.g. Andersson et al. 2012; Ho et al. 2015; Montoli et al. 2020, 2021). The quantity of interest is frequently the cumulative fractional change in spin frequency due to glitches, $\mathcal{A} \propto \sum_i \Delta f_i/f$. An understanding of the completeness of the glitch sample is essential to understanding the uncertainty on \mathcal{A} , and by extension understanding the implications of measured values of \mathcal{A} on the underlying physics.

ACKNOWLEDGEMENTS

The authors are most grateful to the UTMOST team for their hard work in collecting the data which forms the first UTMOST open data release. The Molonglo Observatory is owned and operated by the University of Sydney

with support from the School of Physics and the University. Parts of this research are supported by the Australian Research Council (ARC) Centre of Excellence for Gravitational Wave Discovery (OzGrav) (project number CE170100004) and ARC Discovery Project DP170103625. L. Dunn is supported by an Australian Government Research Training Program Scholarship and by the Rowden White Scholarship. This work was performed on the OzSTAR national facility at Swinburne University of Technology. The OzSTAR program receives funding in part from the Astronomy National Collaborative Research Infrastructure Strategy (NCRIS) allocation provided by the Australian Government.

DATA AVAILABILITY

The public UTMOST data underlying this work are available at <https://github.com/Molonglo/TimingDataRelease1/>. The other data underlying this work will be shared on reasonable request to the corresponding author.

REFERENCES

- Anderson P., Itoh N., 1975, *Nature*, 256, 25
- Andersson N., Glampedakis K., Ho W. C. G., Espinoza C. M., 2012, *Physical Review Letters*, 109, 1
- Arzoumanian Z., Nice D. J., Taylor J. H., Thorsett S. E., 1994, *The Astrophysical Journal*, 422, 671
- Atwood W. B., et al., 2009, *The Astrophysical Journal*, 697, 1071
- Backer D. C., 1970, *Nature*, 228, 1297
- Bailes M., et al., 2017, *Publications of the Astronomical Society of Australia*
- Basu A., Joshi B. C., Krishnakumar M. A., Bhattacharya D., Nandi R., Bandhopadhyay D., Char P., Manoharan P. K., 2020, *Monthly Notices of the Royal Astronomical Society*, 491, 3182
- Camilo F., et al., 2018, *The Astrophysical Journal*, 856, 180
- Carlin J. B., Melatos A., 2019, *Monthly Notices of the Royal Astronomical Society*, 488, 4890
- Chukwude A. E., Urama J. O., 2010, *Monthly Notices of the Royal Astronomical Society*, 406, 1907
- Cordes J. M., Downs G., 1985, *Astrophysical Journal Supplement Series*, 59, 343
- Cordes J. M., Helfand D., 1980, *The Astrophysical Journal*, 15, 640
- Dodson R. G., McCulloch P. M., Lewis D. R., 2002, *The Astrophysical Journal Letters*, 564, L85
- Dunn L., Lower M. E., Melatos A., 2021, *Monthly Notices of the Royal Astronomical Society*, 504, 3399
- Espinoza C. M., Lyne A. G., Stappers B. W., Kramer M., 2011, *Monthly Notices of the Royal Astronomical Society*, 414, 1679
- Espinoza C. M., Antonopoulou D., Stappers B. W., Watts A., Lyne A. G., 2014, *Monthly Notices of the Royal Astronomical Society*, 440, 2755
- Espinoza C. M., Antonopoulou D., Dodson R., Stepanova M., Scherer A., 2021, *A&A*, 647, A25
- Fuentes J. R., Espinoza C. M., Reisenegger A., Shaw B., Stappers B. W., Lyne A. G., 2017, *Astronomy & Astrophysics*, 608, A131
- Gancio G., et al., 2020, *Astronomy & Astrophysics*, 633, A84
- Goncharov B., et al., 2021, *Monthly Notices of the Royal Astronomical Society*, 502, 478
- Haskell B., Melatos A., 2015, *International Journal of Modern Physics D*, 24, 1530008

Helfand D. J., Manchester R. N., Taylor J. H., 1975, *The Astrophysical Journal*, 198, 661

Ho W. C. G., Espinoza C. M., Antonopoulou D., Andersson N., 2015, *Science Advances*, 1, e1500578

Ho W. C. G., et al., 2020, *Monthly Notices of the Royal Astronomical Society*, 498, 4605

Hobbs G. B., Edwards R. T., Manchester R. N., 2006, *Monthly Notices of the Royal Astronomical Society*, 369, 655

Hobbs G., Lyne A. G., Kramer M., 2010, *Monthly Notices of the Royal Astronomical Society*, 402, 1027

Hotan A. W., van Straten W., Manchester R. N., 2004, *Publ. Astron. Soc. Australia*, 21, 302

Howitt G., Melatos A., Delaigle A., 2018, *The Astrophysical Journal*, 867, 60

Jankowski F., et al., 2015, *The Astronomer's Telegram*, 8298

Jankowski F., et al., 2016, *The Astronomer's Telegram*, 9054

Jankowski F., et al., 2019, *Monthly Notices of the Royal Astronomical Society*, 484, 3691

Jankowski F., Keane E. F., Stappers B. W., 2021, *MNRAS*, 504, 406

Janssen G. H., Stappers B. W., 2006, *Astronomy & Astrophysics*, 457, 611

Kerr M., 2019, *Astronomer's Telegram*, 12481

Lentati L., Alexander P., Hobson M. P., Feroz F., van Haasteren R., Lee K. J., Shannon R. M., 2014, *Monthly Notices of the Royal Astronomical Society*, 437, 3004

Levin L., et al., 2010, *The Astrophysical Journal*, 721, L33

Lower M. E., et al., 2018, *Research Notes of the AAS*, 2, 139

Lower M. E., et al., 2020, *Monthly Notices of the Royal Astronomical Society*, 494, 228

Lower M. E., et al., 2021, *MNRAS*, 508, 3251

Lyne A., Graham-Smith F., 2012, *Pulsar Astronomy*. Cambridge University Press

Lyne A. G., Shemar S. L., Graham Smith F., 2000, *Monthly Notices of the Royal Astronomical Society*, 315, 534

Lyne A., Hobbs G., Kramer M., Stairs I., Stappers B., 2010, *Science*, 329, 408

Melatos A., Peralta C., Wyithe J. S. B., 2008, *The Astrophysical Journal*, 672, 1103

Melatos A., Howitt G., Fulgenzi W., 2018, *The Astrophysical Journal*, 863, 196

Melatos A., Dunn L. M., Suvorova S., Moran W., Evans R. J., 2020, *The Astrophysical Journal*, 896, 78

Montoli A., Antonelli M., Pizzochero P. M., 2020, *Monthly Notices of the Royal Astronomical Society*, 492, 4837

Montoli A., Antonelli M., Haskell B., Pizzochero P., 2021, *Universe*, 7, 8

Palfreyman J., 2016, *Astronomer's Telegram*, 9847

Parthasarathy A., et al., 2019, *Monthly Notices of the Royal Astronomical Society*, 000, 1

Rabiner L. R., 1989, *Proceedings of the IEEE*, 77, 257

Sarkissian J., Hobbs G., Reynolds J., Palfreyman J., Olney S., 2019, *Astronomer's Telegram*, 12466

Shannon R. M., Lentati L. T., Kerr M., Johnston S., Hobbs G., Manchester R. N., 2016, *Monthly Notices of the Royal Astronomical Society*, 459, 3104

Shemar S. L., Lyne A. G., 1996, *Monthly Notices of the Royal Astronomical Society*, 282, 677

Singha J., Basu A., Krishnakumar M. A., Joshi B. C., Arumugam P., 2021, *MNRAS*, 505, 5488

Venkatraman Krishnan V., et al., 2020, *Monthly Notices of the Royal Astronomical Society*, 492, 4752

Verbiest J. P. W., Shaifullah G. M., 2018, *Classical and Quantum Gravity*, 35, 133001

Wang N., Manchester R. N., Johnston S., 2007, *Monthly Notices of the Royal Astronomical Society*, 377, 1383

Yu M., Liu Q., 2017, *Monthly Notices of the Royal Astronomical Society*, 3041, 3031

Yu M., et al., 2013, *Monthly Notices of the Royal Astronomical Society*, 429, 688

APPENDIX A: FOLLOW-UP ANALYSIS OF VETOED CANDIDATES

In Section 4 we describe the vetoing of three candidates. Given that these vetos proceed by removing the ToAs bracketing each of the candidates, there is a chance that genuine glitch events may be discarded by this procedure, if the glitch is close to the limit of detectability. In this appendix we investigate each of the vetoed candidates in more detail, with the aim of clarifying their origin.

A1 PSR J0742–2822

The case of PSR J0742–2822 turns out to be straightforward. The dispersion measure (DM) in the ephemeris file provided in the UTMOST data release was mistakenly quoted as 681 pc cm^{-3} , whereas the correct value is 74 pc cm^{-3} . A large error in the DM can produce significant scatter in the timing residuals, as even small variations in the central frequency of each observation lead to large corrections to the ToAs. After correcting the DM in the ephemeris, we find that the scatter in the residuals in the vicinity of the candidate is reduced by a factor of 20. Finally, we re-run the HM analysis with the updated DM value and find no candidate. Hence we reject the initial candidate as non-astrophysical.

A2 PSR J1105–6107

Inspection of the timing residuals surrounding the candidate in PSR J1105–6107 reveals no obvious features, and inspection of the raw archives similarly reveals no disturbance in the vicinity of the candidate. As a consistency check, we re-generate the ToAs for PSR J1105–6107 using PSRCHIVE (Hotan et al. 2004) and re-run the HMM analysis. No candidate is returned, and we thus reject the candidate as non-astrophysical.

We are unable to identify a clear reason for the discrepancy between the ToAs in the data release and the re-generated set. As we are aware, both the archives containing the folded observations and the standard profile used to generate the times of arrival have not changed between the UTMOST data release and the re-generation described here. However, records of the UTMOST data release preparation are not sufficiently detailed to allow us to check this, and it is possible that the profile used to generate the ToAs in the UTMOST data release was not optimal (e.g. not sufficiently smoothed).

A3 PSR J1359–6038

Inspection of the timing residuals surrounding the candidate in PSR J1359–6038 reveals that a single ToA at MJD 58190.7 is displaced away from the rest of the surrounding ToAs by approximately 0.4 ms. This is significant compared to the uncertainty on this ToA of $60 \mu\text{s}$. To check whether this displaced ToA is due to conditions at the observatory,

we inspect the timing residuals of other pulsars that were observed no more than twelve hours before or after the ToA in question. We identify multiple pulsars in which the observation nearest MJD 58190.7 is displaced by approximately the same amount in the same direction, for example PSRs J1146–6030, J1600–3053⁸, and J1644–4559. Thus we conclude that the candidate in PSR J1359–6038 is due to local conditions at the observatory and has no astrophysical origin.

APPENDIX B: SYNTHETIC DATASET GENERATION AND UPPER LIMIT ESTIMATION

In order to set frequentist upper limits we perform injection studies for each pulsar. We first outline the procedure for generating a single synthetic dataset for one object, which is based on a given UTMOST dataset (i.e. with identical ephemeris, observing cadence, and ToA uncertainties), with a glitch of size Δf injected.

(i) A glitch epoch t_g is chosen at random, uniformly distributed between the second and second-last ToAs. Glitches which occur in either the first or last ToA gap are indistinguishable from a single outlier ToA due to some external factor, so we do not consider them when setting upper limits here.

(ii) A new phase model is generated by LIBSTEMPO which matches the UTMOST phase model, except that a glitch term $\Delta\phi_g(t) = \Theta(t - t_g)\Delta f(t - t_g)$ is added [where $\Theta(t)$ is the Heaviside step function].

(iii) Using the ToAs of the original dataset as a starting point, a new set of ToAs is generated by shifting the original ToAs slightly so that they show zero residuals with respect to the new phase model.

(iv) Noise is introduced into the new set of ToAs at the levels reported in the UTMOST data release. We use the `add_efac`, `add_equad`, and `add_rednoise` functions in LIBSTEMPO, using the EFAC, EQUAD, and red noise parameters reported for each pulsar in the UTMOST data release.

(v) The new phase model and new set of ToAs are saved as a synthetic dataset.

This procedure ensures that the synthetic datasets closely match the true datasets in various important aspects, e.g. basic timing model parameters, observing cadence, and noise characteristics.

The procedure for estimating the probability of detection for a glitch size Δf [denoted $P_d(\Delta f)$] in a single pulsar is straightforward:

(i) Generate 100 synthetic datasets with a glitch of size Δf injected, according to the procedure in the paragraph above.

(ii) Analyse each dataset with the HMM following the method outlined in Section 3.

(iii) For each dataset, determine the Bayes factor K between the model $M_1(k_{inj})$ with a glitch included in the ToA gap indexed by k_{inj} corresponding to the injected glitch epoch and the model M_0 with no glitch included.

⁸ In the case of PSR J1600–3053 the displaced ToA was removed manually during the preparation of the public data release.

(iv) The proportion of synthetic datasets with $K > K_{th}$ gives an estimate of $P_d(\Delta f)$.

Finally we give a simple prescription for estimating the value of $\Delta f^{90\%}$ from $P_d(\Delta f^{90\%}) = 0.9$, i.e. the 90% upper limit on the size of undetected glitches in each pulsar.

(i) Choose the starting range of glitch sizes to be $[\Delta f_-, \Delta f_+] = [10^{-9}, 10^{-6}]$ Hz.

(ii) Choose a glitch size Δf by bisecting the range logarithmically, i.e.,

$$\log_{10}(\Delta f) = \log_{10}(\Delta f_-) + [\log_{10}(\Delta f_+) - \log_{10}(\Delta f_-)]/2 \quad (\text{B1})$$

where all the frequencies are understood to be in units of Hz.

(iii) Calculate $P_d(\Delta f)$ as outlined previously.

(iv) If $|P_d(\Delta f) - 0.9| \leq 0.01$, terminate and take Δf as the 90% frequentist upper limit $\Delta f^{90\%}$.

(v) Otherwise, revise the glitch size range as follows:

(a) If $P_d(\Delta f) > 0.9$, set $\Delta f_+ = \Delta f$.

(b) If $P_d(\Delta f) < 0.9$, set $\Delta f_- = \Delta f$.

(vi) Return to step (ii).

This is essentially a binary search over possible upper limits.

APPENDIX C: POSTERIOR DISTRIBUTIONS AND FREQUENCY TRACKS FOR HMM ANALYSES

This appendix collects Figs. C1–C8 showing the sequence of most likely frequencies $\hat{f}(t_n)$ and heatmaps of the frequency posterior distributions $\gamma_f(t_n)$ for the eight pulsars which are followed up with glitch parameter estimation analyses as described in Section 4. The structure of each figure is essentially the same: the left panel shows $\hat{f}(t_n)$ as a function of the MJD, and the right panel shows $\ln[\gamma_f(t_n)]$ as a function of ToA gap index. The values of $\ln[\gamma_f(t_n)]$ have been clipped below to aid readability. The vertical axis in both cases extends over the full f range in the DOI for each analysis. In some cases $\gamma_f(t_n)$ displays multiple peaks; see Section 4.1 and Dunn et al. (2021) for further discussion of this phenomenon. Both $\hat{f}(t_n)$ and $\gamma_f(t_n)$ are obtained using the forward-backward algorithm (Rabiner 1989). We also remind the reader that $\hat{f}(t_n)$ is the sequence of most likely states at each timestep (i.e. it is constructed from the sequence of modes of the posterior distribution of states) – it is not the most likely sequence of states, which may instead be calculated using the Viterbi algorithm (Rabiner 1989). However, the difference between these two sequences is typically small (Melatos et al. 2020), and so we prefer to use $\hat{f}(t_n)$.

We also include in Fig. C9 an illustrative plot showing the frequency derivative posterior distribution $\gamma_{\dot{f}}(t_n)$ from the follow-up analysis of PSR J1371–3744. As mentioned in Section 4, we do not include equivalent plots for every pulsar, as the coarse discretisation of \dot{f} in the DOI leads to relatively uninformative \dot{f} posteriors. In the exemplar plot, $\gamma_{\dot{f}}(t_n)$ shows support over a significant fraction of the DOI, particularly after the glitch occurs at the 103rd ToA, making it difficult to make useful inferences about the evolution of

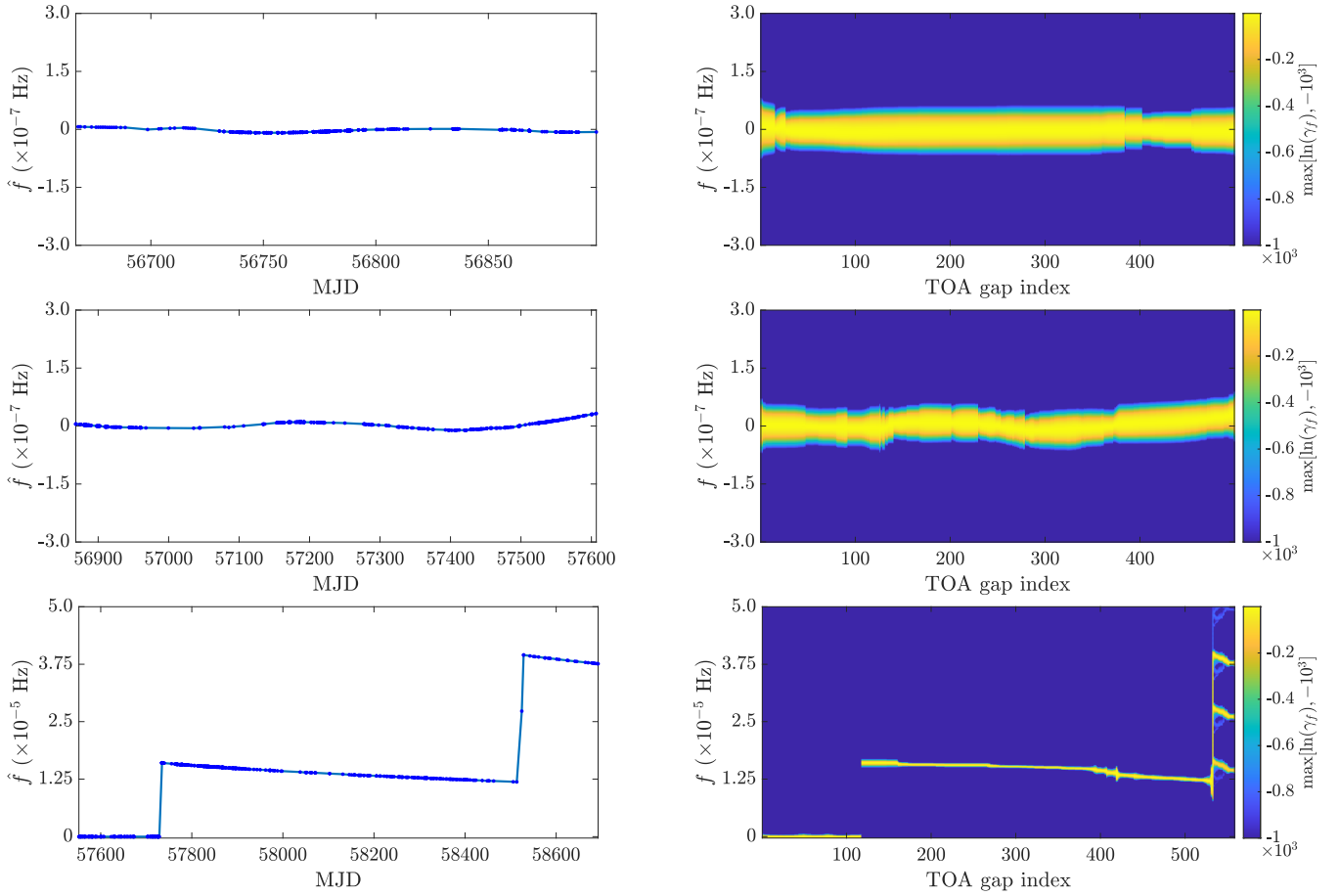


Figure C1. Sequence of most likely frequencies $\hat{f}(t_n)$ (*left*) and heatmap of posterior frequency probability $\ln[\gamma_f(t_n)]$ (*right*) for the HMM follow-up analysis of PSR J0835–4510. Frequency is on the vertical axis in all panels, and the range of the vertical axis is the full range of the DOI. Note that the horizontal axes for the two panels are not exactly the same: the left panels have MJD on the horizontal axis, while the right panels have ToA gap index on the horizontal axis instead, for ease of plotting. The three rows correspond to sections 1, 2 and 3 from top to bottom as described in Table 5.

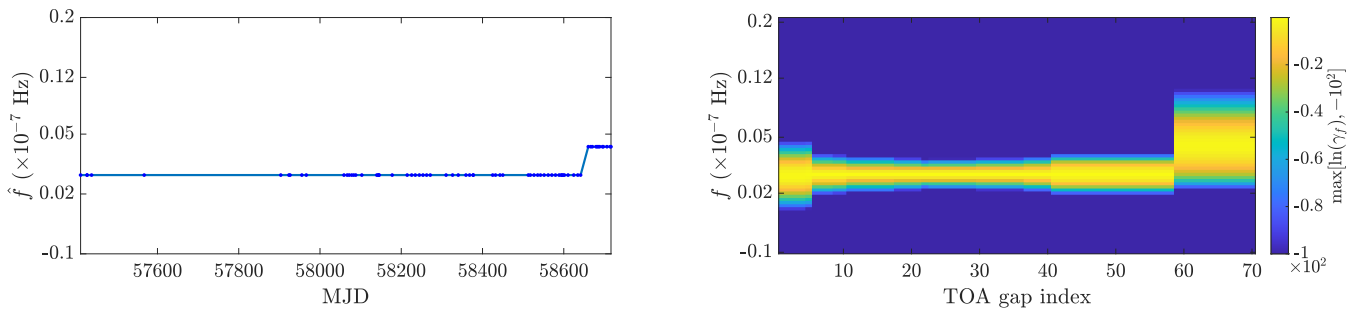


Figure C2. As in Figure C1, but for PSR J1257–1027.

\dot{f} over the dataset. Note that the heatmap shows γ_f , not its natural logarithm, unlike Figs. C1–C8.

This paper has been typeset from a $\text{\TeX}/\text{\LaTeX}$ file prepared by the author.

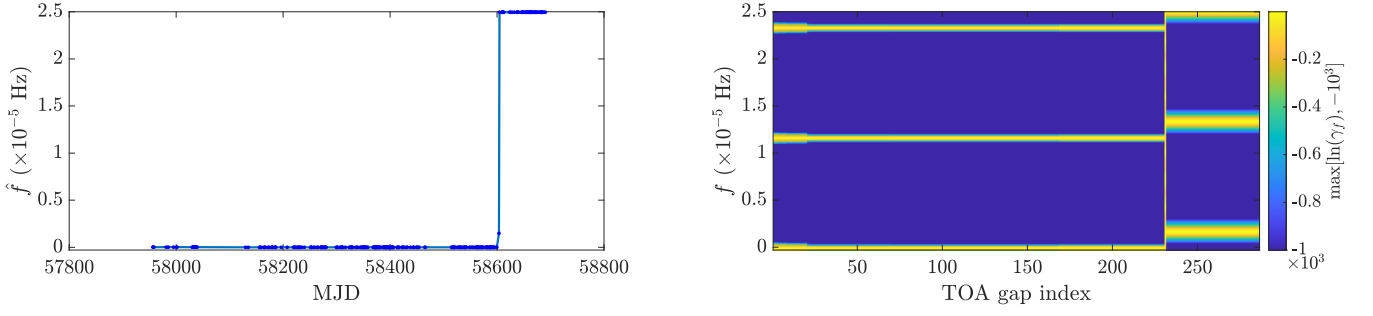


Figure C3. As in Figure C1, but for PSR J1452–6036.

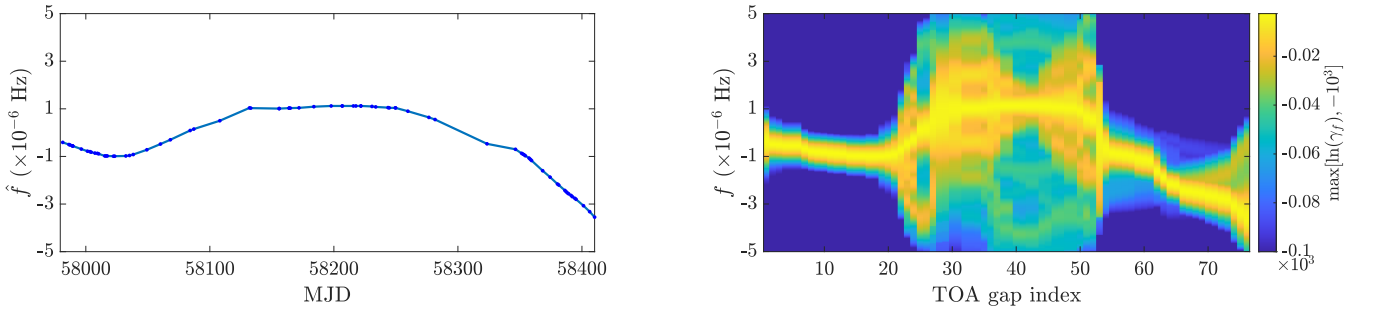


Figure C4. As in Figure C1, but for PSR J1622–4950.

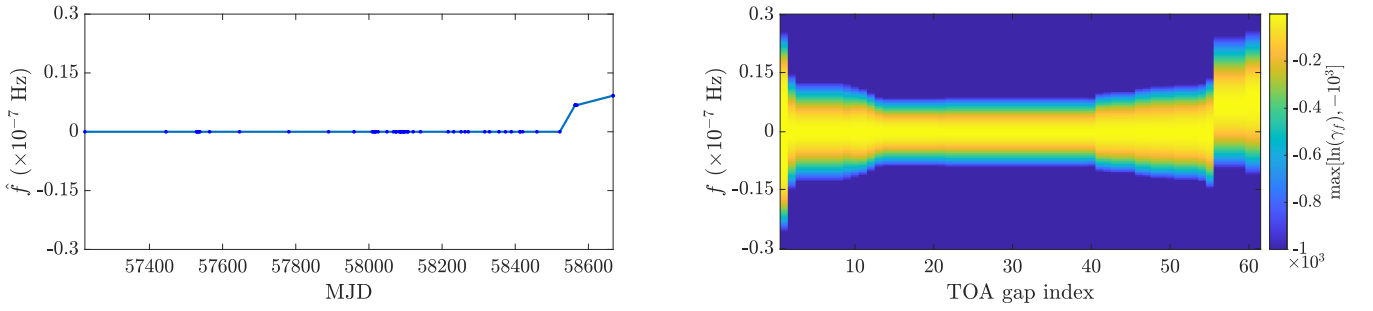


Figure C5. As in Figure C1, but for PSR J1703–4851.

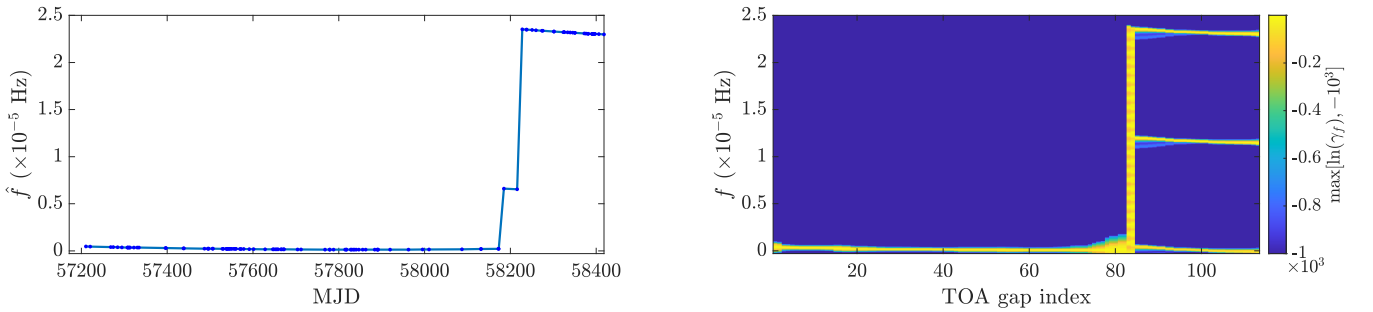


Figure C6. As in Figure C1, but for PSR J1709–4429.

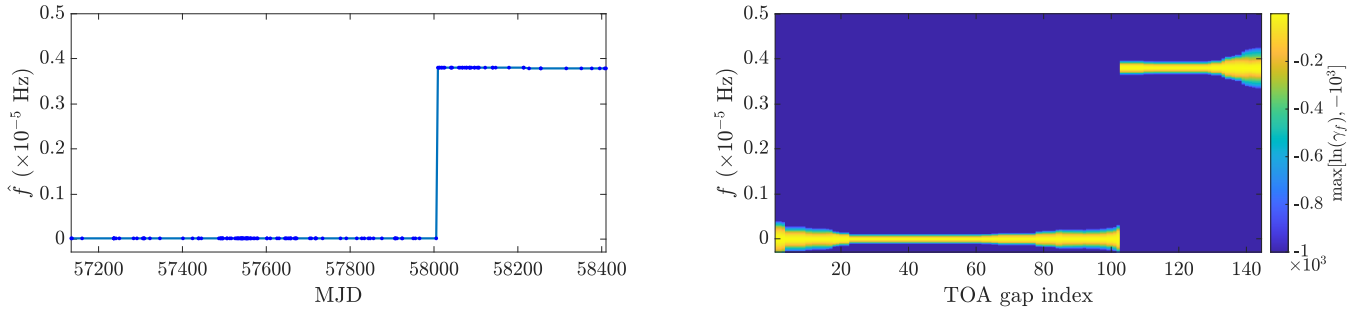


Figure C7. As in Figure C1, but for PSR J1731–4744.

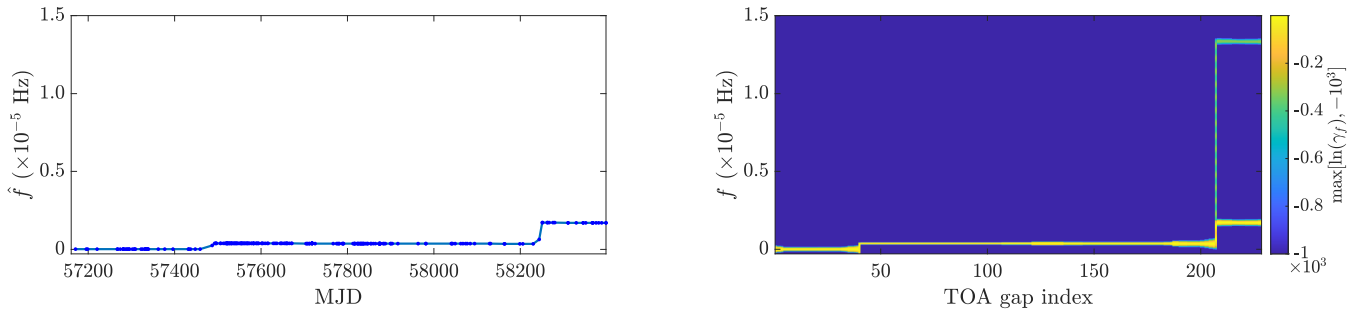


Figure C8. As in Figure C1, but for PSR J1740–3015.

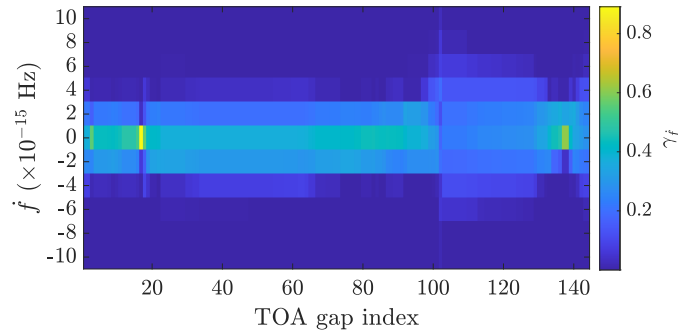


Figure C9. Heatmap of posterior frequency derivative probability $\gamma_f(t_n)$ for the HMM follow-up analysis of J1731–4744.